

Article

Settling of Road-Deposited Sediment: Influence of Particle Density, Shape, Low Temperatures, and Deicing Salt

Steffen H. Rommel ¹, Laura Gelhardt ², Antje Welker ² and Brigitte Helmreich ^{1,*}

¹ Chair of Urban Water Systems Engineering, Technical University of Munich, Am Coulombwall 3, 85748 Garching, Germany; sww@tum.de

² Fachgebiet Siedlungswasserwirtschaft und Hydromechanik (Institute of Urban Water Management and Hydromechanics), Frankfurt University of Applied Sciences, Nibelungenplatz 1, 60318 Frankfurt am Main, Germany; Laura.Gelhardt@fb1.fra-uas.de (L.G.); antje.welker@fb1.fra-uas.de (A.W.)

* Correspondence: b.helmreich@tum.de

Received: 7 October 2020; Accepted: 5 November 2020; Published: 7 November 2020



Abstract: Separation of particulate matter (PM) is the most important process to achieve a reduction of contaminants present in road runoff. To further improve knowledge about influencing factors on the settling of road-deposited sediment (RDS), samples from three sites were collected. Since particle size distribution (PSD) has the strongest effect on settling, the samples were sieved to achieve comparable PSDs so that the effects of particle density, shape, fluid temperature, and deicing salt concentration on settling could be assessed using settling experiments. Based on the experimental data, a previously proposed model that describes the settling of PM was further developed and validated. In addition, RDS samples were compared to a standard mineral material, which is currently in use to evaluate treatment efficiency of stormwater quality improvement devices. The main finding was that besides PSD, particle density is the most important influencing factor. Particle shape was thoroughly described but showed no significant improvement of the prediction of the settled mass. Temperature showed an effect on PM settling; deicing salts were negligible. The proposed models can sufficiently predict the settling of RDS in settling column experiments under varying boundary conditions and are easily applicable.

Keywords: road runoff; road-deposited sediment; sedimentation; stormwater treatment; deicing salt; storm water control measure; modeling

1. Introduction

Road-deposited sediment (RDS) is an important source of contamination in urban environments [1–3]. RDS contains inorganic and organic pollutants such as heavy metals (e.g., Cu, Zn, Pb, Cd, Cr, Ni) and polycyclic aromatic hydrocarbons (PAH) [4–6]. To mitigate the effect caused by RDS on the environment, stormwater control measures (SCMs) such as stormwater quality improvement devices (SQIDs) and detention basins are designed to retain RDS from stormwater runoff by sedimentation or filtration [7,8]. However, previous studies have shown that SCMs exhibit reduced retention efficiency under winter conditions caused by low temperature and deicing salts [9–11]. To design the sedimentation stages of SQIDs, knowledge about particle characteristics and settling velocity distributions of RDSs is crucial [12,13], especially to separate fine particles and particles with low density, which show an increased contaminant load [5,14–17]. In addition, the influence on settling by particle size distribution (PSD), particle density, and runoff event-specific properties, such as first

flush and runoff volume and intensity, has been comprehensively studied [18–23]. Other factors such as temperature, deicing salt, and particle shape have not been sufficiently investigated yet.

The first predictions of Rommel and Helmreich [9] indicated that the presence of deicing salt (sodium chloride) had a negligible influence on the retention of particles. However, reducing the temperature from 20 to 5 °C was shown to decrease the removal efficiency of RDS in a sedimentation shaft by up to 8%. To calculate densities and viscosities of various deicing salt solutions, the equations of Laliberté [24,25] were adapted. The order of influencing factors for the sedimentation was found to be particle size distribution >> overflow rate > particle density > temperature. Even though the results of a 20-month monitoring of full-scale sedimentation indicated worse particulate matter (PM) separation in the cold season, the data were not sufficient to quantify the influencing factors. Thus, lab-scale experiments, with a comparable setup, would be necessary to exclude other environmental influences on the sedimentation, which are always present under real conditions (i.e., varying discharge rates and PM properties, stratification and mixing of water with different temperature and deicing salt concentrations), and validate the modeling predictions.

There are various protocols to determine settling velocity distribution [12,17,26–28]; however, they have not been utilized yet to quantify the influence of temperature and deicing salts on the settling velocity of RDSs. Commonly, artificial test materials are used to reduce variations of PM properties [17]. Gelhardt et al. [17] developed a laboratory method to measure and compare the settling behavior of artificial and real particle collectives with a reproducible PSD. Real RDSs were used in the study, yet the focus was on method development and not on the influence of boundary conditions on the settling behavior of RDS. Ying and Sansalone [29] were, to our best knowledge, the first authors who adapted settling experiments to study the effect of temperature and concentration of deicing salts on the settling of PM from urban runoff. They concluded—based on a computational fluid dynamics (CFDs) model of a hydrodynamic separator—that temperature and deicing salt is negligible to describe the discrete settling of PM.

As these results partly differ from the results of Rommel and Helmreich [9] and the investigation was done with the model of a hydrodynamic separator and not a basic sedimentation unit, the settling column experiments proposed by Gelhardt et al. [17] were adapted to further evaluate the effects of particle density, shape, temperature, and deicing salt (sodium chloride, NaCl) concentration. Based on these results, the model proposed by Rommel and Helmreich [9] was further developed to be able to model settling experiments and was consecutively validated.

Hence, RDSs were thoroughly characterized, and the effects of the influencing factors studied in settling column experiments. Furthermore, the nonspherical shape of RDS was evaluated using dynamic image analysis and considered in an additional model. Since the determination of particle sphericity is still difficult to measure for engineering purposes [30,31], sphericity was approximated by 2D projections of the particles captured using dynamic image analysis.

There exist recent studies that have determined the drag or settling velocity of irregular particles based on more complex descriptions of particle shapes [32–34]. However, our approach was to simplify the particle description and model so that it is more accessible for the engineering purposes of stormwater treatment. In addition, the standard mineral material, which is in use for the technical approval of SQIDs in Germany [35,36], was compared to RDSs.

2. Materials and Methods

2.1. Materials—Study Site and Characterization

Three RDS samples were collected using a vacuum cleaner (DCV 582, Dewalt Deutschland, Idstein, Germany) at three locations in Frankfurt, Germany, with varying annual average daily traffic (AADT) and land usage, which affects RDS properties (Table 1). Solids on the road surface were loosened by means of a paintbrush. In addition to the RDS, the standard mineral material MiW4 (Millisil W4, Quarzwerke, Haltern, Germany) was used for comparison to the RDSs. MiW4 is a milled quartz

material, which is in use in the German technical approval procedure of SQIDs to assess PM separation efficiency. It reflects the PSD of road runoff [17,35]. Prior to sieving, the samples were dried at 105 °C until constant weight was achieved. Fractions > 2 mm were removed using a stainless steel sieve.

Table 1. Characteristics of sampling site and studied materials (< 250 µm), LOI (loss on ignition), and ρ_s (particle density) were calculated after fractionation and recomposition, as described below.

Sample	Location	Coordinate	Sampling Date	AADT (Vehicles/d)	LOI (%)	ρ_s (g cm ⁻³)
MiW4 ^a	–	–	–	–	<0.1	2.65
ECL	Eckenheimer Landstraße	50°07′57.2″ N 8°41′03.5″ E	18 July 2017	8500	7.6	2.60
GBS ^b	Glauburgstraße	50°07′38.6″ N 8°41′28.0″ E	6 April 2017 ^b 12 April 2017 ^b 21 April 2017 ^b	9600	17.5	2.32
FRS	Frauensteinstraße	50°07′51.1″ N 8°40′47.7″ E	17 October 2017	150	22.2	2.25

^a Standard mineral material; ^b The sample GBS was a composite sample of three samples due to low quantity.

To achieve a comparable PSD of all studied RDS, the samples were sieved using a sieve stack with the mesh sizes 1000, 500, 250, 200, 160, 125, 100, 63, and 40 µm, respectively. Subsequently, the obtained fractions were again dried at 105 °C and merged with the percentages summarized in Table 2. The sieving process is described in detail in Gelhardt et al. [17].

Table 2. Particle size distribution of the road-deposited sediments used within this study.

Size Fraction (µm)	Weight (%)	Cumulative Weight (%)
200–250	4	100
160–200	6	96
125–160	12	90
100–125	8	78
63–100	21	70
40–63	15	49
<40	34	34

The sieve fractions were characterized by measuring particle density ρ_s and the loss on ignition (LOI). The ρ_s was determined using a gas pycnometer (Quantachrome Microultrapyk 1200 eT, Anton Paar QuantaTec, Boynton Beach, USA) with helium (5.0, Air Liquide, Germany, Purity ≥ 99.999%), according to DIN 66137-2. To determine the LOI, the dried materials were ignited in a muffle furnace at 550 °C for 2 h (DIN EN 15169). LOI is an indicator to assess the organic fraction of the RDS. The characteristics of the studied materials are summarized in Table 1.

Particle size and shape were determined by dynamic image analysis according to ISO 13322-2 (2006) using the system QICPIC+LIXELL+LIQXI (Sympatec, Clausthal-Zellerfeld, Germany). The module M5 was used, with a measuring range between 1.8 and 3755 µm. Prior to the analysis, the samples were dispersed in deionized water using ultrasonic homogenization at 50% amplitude for 60 s (Sonopuls HD 2200.2, Bandelin, Berlin, Germany). Approximately 0.25 g of the sample was applied to 200 mL of deionized water to achieve an optimum concentration of < 2% during the measurement. Settings of the device were 800 U min⁻¹ stirring rate, 125 U min⁻¹ recirculation rate, 30 Hz frame rate, and 60 s acquisition time. These settings were optimized for the reproducibility of the PSD of MiW4. Data were analyzed using the proprietary software PAQXOS (Sympatec, Clausthal-Zellerfeld, Germany). Based on suggestions by the manufacturer of the device, particles <5.4 µm were discarded for size analysis and particles <16 µm were discarded for the shape analysis to assure sufficient image resolution. One million particles were analyzed for each sample due to the aforementioned thresholds; particle

counts decreased. The following size and shape parameters were determined: the area equivalent circle diameter (d_{eq}); the Riley circularity $\varphi_{Riley} = \sqrt{D_i/D_c}$ [37], where D_i is the diameter of the largest inscribed circle and D_c is the smallest circumscribed circle; the aspect ratio $AR = x_{Fmin}/x_{Fmax}$, where x_{Fmin} is the minimal Feret diameter and x_{Fmax} is the maximal Feret diameter (ISO 9276-6:2008). Values of $\varphi_{Riley} > 1$ were substituted by 1, since the value 1 would be the value of a circle and values >1 were caused by measuring uncertainties. Numerous other definitions of circularity exist; we selected φ_{Riley} because it was suggested by Bagheri et al. [38] as a predictor for particle sphericity. As the experiments were focused on the settled mass, size and shape distributions were weighted by the mass fractions of the particles. These were determined under the assumptions of constant density for each sample and a spherical particle shape with the diameter d_{eq} .

2.2. Settling Experiments

The settling experiment utilized in this study is based on the method proposed by Gelhardt et al. [17], which was adapted from the method, developed by the company UFT [28]. A comprehensive description can be found in Gelhardt et al. [17].

In the experiments, glass columns with a length of 780 mm and an inner diameter of 50 mm were used. The settling height was 760 mm. This method is a floating layer method [27]. Since this study did not intend to determine settling velocity distributions, only the settled fraction after 4 min was evaluated. This fraction exhibits a settling velocity of $\geq 11.4 \text{ m h}^{-1}$, which approximately reflects the fraction $\geq 63 \text{ }\mu\text{m}$ of mineral material with a density of 2.65 g cm^{-3} .

Prior to each experiment, the columns filled with deionized water (DI water) were adjusted to either 21.0 ± 0.1 or $10.0 \pm 0.1 \text{ }^\circ\text{C}$ in a climate chamber (Thermo-TEC, Rochlitz, Germany), depending on the experiment. Additional experiments with 20 g L^{-1} NaCl (VWR, p.A., CAS: 7647-14-5; $w_{NaCl} = 0.02$) were performed to assess the influence of deicing salt at $10 \text{ }^\circ\text{C}$. This NaCl concentration can be considered an extreme value for deicing salt concentration in road runoff [39,40]. The names of the experiments used in the remaining text consist of the following information: material, temperature and NaCl concentration (e.g., MiW4, $21 \text{ }^\circ\text{C}$, 0 g/L).

Temperature and electrical conductivity (EC) were measured according to standard method 2510 B [41]. A suspension containing 0.5 g RDS or MiW4 was applied in the experiments. The suspension was prepared prior to the experiment in 15 mL glass vials by adding 10 mL of the same solution in the columns to the RDS or MiW4 . The suspension was homogenized by 1 min of manual shaking. The settling experiments were conducted without delay after the preparation of the suspension. Thus, no alteration of the samples can be expected [18]. The sample of the settled fraction was withdrawn after 4 min . The mass of the settled fraction was determined after the evaporation of the withdrawn sample according to standard method 2540 B [41]. Since dissolved NaCl would severely bias the results, the samples of experiments with $w_{NaCl} > 0$ were analyzed using membrane filtration with $0.45 \text{ }\mu\text{m}$ membrane filters (cellulose nitrate, Sartorius, Type 113, 47 mm diameter) in accordance with standard method 2540 D [41]. Both methods for the determination of the settled fraction, either evaporation or filtration, were in good agreement with each other (cf. Figure S1). To determine the nonsettled fraction, the water remaining in the column after the experiment was filtered and the total suspended solids (TSS) were determined according to standard method 2510 B [41]. The lost particulate mass was calculated by the initial particulate mass subtracted by the sum of the settled and nonsettled particulate mass. In the experiments, $3.3\% \pm 1.9\%$ of the particulate mass was lost; this was not considered in the determination of the settled mass fractions. Each experiment was conducted in triplicate.

2.3. Modeling of Settling Experiments

The entire model was implemented in Python with the packages Pandas, Matplotlib, SciPy, and Seaborn [42–45]. It is accessible in Supplementary Material A.

The PSD of the preprocessed RDSs were modeled using a Weibull cumulative probability density function [9,46,47], following Equation (1)

$$W(d, \lambda, \kappa) = 1 - e^{(-\frac{d}{\lambda})^\kappa} \quad (1)$$

where $W(d, \lambda, \kappa)$ = mass fraction less than d (-); d = particle diameter (μm); λ = shape parameter (-); κ = scale parameter (-) [9,46,47]. The determined λ and κ were 85.09 and 1.247 for the used PSD. These parameters were determined by the curve fitting in Matlab R2019a (MathWorks, Natick, USA) using the upper particle diameters of the fractions and nonlinear least squares method with the Trust-Region algorithm ($R^2 = 0.998$, $\text{RMSE} = 0.016$). The λ and κ are within the range of previously reported values for PSD in urban stormwater or RDS [9,47]. The PSD was described in the range of 0–250 μm , with 1- μm increments (Figure S2).

Density (ρ_f), dynamic viscosity (η_f), and kinematic viscosity (ν_f) of the evaluated fluids at varying fluid temperatures (t) and NaCl mass fractions (w_{NaCl}) were determined using the equations established by Laliberté et al. [24,25], as described in Rommel and Helmreich [9].

The terminal settling velocity (w) was determined by means of different approaches, with further consideration of influencing factors for each particle diameter (d), ρ_s , t , w_{NaCl} , and sphericity (ϕ) for Model C. In addition, d was approximated by the Weibull fit of the PSD since the diameter of isotropic-shaped particles can be approximated by the screen size [48].

- Model A: Spherical particles
- Model B: Spherical particles with consideration of the withdrawn sample volume
- Model C: Nonspherical particles

The different models are explained in Sections 2.3.1–2.3.3. All models used the simplification of constant ρ_s (and ϕ for Model C) with respect to particle size. The models used the respective ρ_s and ϕ of the samples used in the experiments. Furthermore, they solely considered discrete settling without the interaction of the particles and no wall effect. Since the PSD was previously defined, a continuous settling velocity distribution was derived for each experiment.

To determine the mass of the settled fraction, the mass fraction at the critical settling velocity (w_{crit}) was calculated by linear interpolation. All settled particles exhibit a settling velocity greater or equal than w_{crit} . The settled mass fraction was determined by the difference of 1 and the mass fraction at w_{crit} .

2.3.1. Model A: Spherical Particles

Model A determined w (m s^{-1}) using the explicit formulas (Equations (2)–(6)) proposed by Cheng [49] for spherical particles in the subcritical region ($\text{Re} < 2 \cdot 10^5$)

$$\Delta = (\rho_s - \rho_f) / \rho_f \quad (2)$$

$$d_* = (\Delta g / \nu_f^2)^{1/3} d \quad (3)$$

$$C_D = \frac{432}{d_*^3} (1 + 0.022d_*^3)^{0.54} + 0.47 [1 - \exp(-0.15d_*^{0.45})] \quad (4)$$

$$w_* = \sqrt{4d_* / 3C_D} \quad (5)$$

$$w = w_* (\Delta g \nu_f)^{1/3} \quad (6)$$

where d_* is the dimensionless grain diameter, g is the gravitational acceleration (m s^{-2}), C_D is the drag coefficient (-), and w_* is the dimensionless settling velocity [49]. Even if Re remains in the low region (< 10), this method avoids the necessity of checking Re during the calculation since it is valid for $\text{Re} < 2 \cdot 10^5$.

2.3.2. Model B: Spherical Particles with Consideration of the Withdrawn Sample Volume

Model B is based on Model A and additionally considers the withdrawn sample volume. Since additional water will be withdrawn with the sediment, not-yet-settled particles will be withdrawn as well. Thus, w_{crit} needs to be reduced with respect to the withdrawn sample volume. This was considered by reducing w_{crit} by the height of the truncated cone (h_{cone}) with the same shape as the utilized glass columns and the volume of the withdrawn sample; h_{cone} of each experiment was determined following Equation (7).

$$h_{\text{cone}} = 5^{2/3} \sqrt[3]{\frac{12V_{\text{sample}}}{\pi} + 5} - 5 \text{ for } 0 < V_{\text{sample}} \leq 162.32 \text{ mL} \quad (7)$$

where V_{sample} is the measured withdrawn sample volume of each experiment in mL and h_{cone} is the height of the truncated cone in cm. The determined h_{cone} was used to adjust w_{crit} to simulate the results of the experiments following Equation (8)

$$w_{\text{crit}} = \frac{76 - h_{\text{cone}}}{0.417} \quad (8)$$

where w_{crit} is the critical settling velocity in m s^{-1} , which is the minimal settling velocity of the particles-withdrawn sample after 4 min, and h_{cone} the height of the truncated cone with the same shape as the utilized glass columns and the volume of the withdrawn sample in mL.

2.3.3. Model C: Nonspherical Particles

To consider the influence of a nonspherical particle shape, Model C included the average sphericity of each RDS determined by dynamic image analysis. Since dynamic image analysis only delivers 2D projections of the particles, the sphericity of the particles (ϕ) was approximated by the circularity of the 2D projections of the particles, as proposed by Bagheri et al. [38]. Settling velocity of the nonspherical particles was predicted using the formulas proposed by Haider and Levenspiel [48] (Equations (9)–(11)) since it is an explicit and simple solution. Furthermore, it shows an acceptable average error [50].

$$d_* = d \left[\frac{g\rho_f(\rho_s - \rho_f)}{\eta_f^2} \right]^{1/3} \quad (9)$$

$$w_* = \left[\frac{18}{d_*^2} + \frac{2.3348 - 1.7439\phi}{d_*^{0.5}} \right]^{-1} \text{ for } 0.5 \leq \phi \leq 1 \quad (10)$$

where ϕ was approximated by the circularity of the 2D projections of the particles [30,38]. Bagheri et al. [38] suggested the use of ϕ_{Riley} for particles with a nonvesicular surface. Based on dynamic image analysis, the particles of the analyzed RDSs showed a nonvesicular surface; thus, the mass fraction weighted median of ϕ_{Riley} was used to approximate ϕ .

$$w = w_* \left[\frac{\rho_f^2}{g\eta_f(\rho_s - \rho_f)} \right]^{-1/3} \quad (11)$$

2.4. Statistics

All statistical methods were implemented using Python with the packages Pandas 1.0.5 [43], Scipy 1.5.0 [42], Scikit-learn 0.23.1 [51], and Statsmodel 0.11.1 [52]. Data was visualized using the packages Matplotlib 3.2.2 [44] and Seaborn 0.11.0 [45]. Hypothesis testing was conducted using a two-sided *t*-test with a significance level of 5%. The error of the predicted settled fraction was assessed using the mean absolute error and the maximum residual error.

3. Results and Discussion

3.1. Particle Size and Shape

By using dynamic image analysis, it was possible to obtain PSDs of the analyzed samples (Figure 1a). The mass fraction weighted medians of d_{eq} for ECL, FRS, GBS, and MiW4 were 72, 85, 74, and 73 μm , respectively. A minor difference between MiW4 and the nonartificial RDSs was revealed. In the fraction below approximately 50 μm , MiW4 showed a greater mass fraction of smaller particles compared to all RDSs. For $d_{eq} > 50 \mu\text{m}$, all materials showed good agreement with the Weibull PSD, which is based on the target PSD of the sieving process (c.f. Section 2.1.) and will be used for the consecutive modeling of settling. Thus, discrepancies between experimental and modeled results for the RDSs can be attributed to the deviation of the present PSDs and the Weibull PSD. As the smallest mesh size was 40 μm , the deviation in the small particle size fraction was anticipated. Consequently, this is one potential source of deviation between predicted and measured settled mass fractions. In order to analyze this fine fraction, future experiments should adopt an addition nylon sieve with a 20- μm mesh size [53].

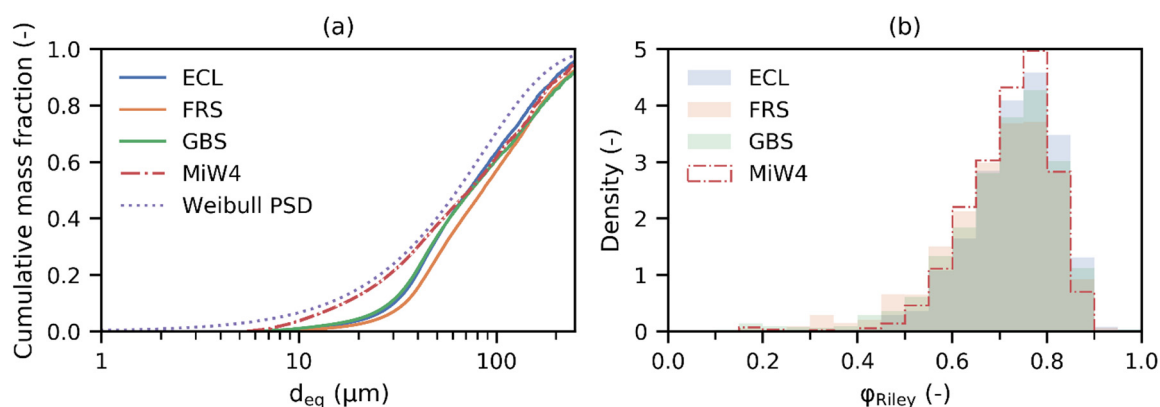


Figure 1. (a) Particle size distribution (PSD) of the analyzed samples and the fitted Weibull PSD used for the subsequent modeling, particle count: Eckenheimer Landstraße (ECL) $n = 515,545$; Frauensteinstraße (FRS) $n = 593,302$; Glauburgstraße (GBS) $n = 540,036$; MiW4 $n = 501,254$. (b) Mass fraction weighted histogram of ϕ_{Riley} of the analyzed samples, particle count: ECL $n = 130,986$; FRS $n = 211,209$; GBS $n = 134,392$; MiW4 $n = 57,973$.

As shown in Figure 2, the RDSs exhibit nonspherical shapes. The mass fraction weighted median ϕ_{Riley} of the analyzed samples were 0.744 for ECL, 0.717 for FRS, 0.732 for GBS, and 0.733 for MiW4, respectively (Figure 1b). According to Blott and Pye [30], the particles of the samples exhibit low to high circularity; thus, a low to high sphericity can be estimated. This finding is supported by the results of Kayhanian et al. [15]. No distinct differences between the samples were observed. ϕ_{Riley} was almost constant with respect to d_{eq} ; however, with decreasing particle size, the range of ϕ_{Riley} was wider (Figure S3). In addition, MiW4 showed a narrower distribution of ϕ_{Riley} with respect to d_{eq} .

The RDS particles were moderately to slightly elongated, with a mass fraction weighted median aspect ratio of 0.62–0.63 [30]. This finding is supported by Gunawardana et al. [14], who reported that RDSs feature particles with an irregular surface and contain a high proportion of elongated particles. Furthermore, the size and shape of the analyzed samples are comparable to tire wear particles [54].



Figure 2. Microscopic images of some road-deposited sediment (RDS) particles of the sample ECL, captured using dynamic image analysis. The particle shape of the other samples was comparable. The images are not scaled.

Based on the observed aspect ratios, the majority of the particles were isometric, with aspect ratios >0.2 (Figure S4), which is a requirement for the approximation of particle sphericity based on 2D projections because particle orientation can bias the determination of the circularity of highly nonisometric particles [31].

3.2. Particle Density with Respect to Particle Size

The particle density of the total preprocessed samples is given in Table 1. In order to evaluate the particle density with respect to particle size, ρ_s of the individual fractions was determined. No distinct trend of decreasing or increasing ρ_s with particle size was observable (Table 3). The density of MiW4 was constant with respect to particle size since it is a milled quartz material. Based on these results, the simplification of constant ρ_s in the modeling is applicable. However, previous studies have shown that smaller particles feature larger organic fractions, resulting in lower ρ_s [15,20].

Table 3. Particle density (ρ_s) of the fractionated samples ECL, FRS, and GBS.

Size Fraction (μm)	ρ_s (g cm^{-3})		
	ECL	FRS	GBS
200–250	2.56	2.25	2.41
160–200	2.54	2.17	2.37
125–160	2.57	2.14	2.31
100–125	2.55	2.18	2.32
63–100	2.61	2.20	2.30
40–63	2.65	2.31	2.31
<40	2.61	2.34	2.32

3.3. Settling Experiments

Using the proposed method, it was possible to quantify the influence of ρ_s , t , and w_{NaCl} . Within 4 min, 30% to 60% of the particles settled.

As predicted by the calculations of Rommel and Helmreich [9], ρ_s showed the greatest impact on the settling at constant PSD (Figure 3). Thus, MiW4 showed the biggest settled fraction overall, followed by ECL, GBS, and FRS in the order of their ρ_s . Furthermore, settling decreased with decreasing temperature for all materials. The addition of deicing salt showed a very minor effect of reducing the settled fraction. However, the experiments with deicing salt were associated with higher uncertainty due to the necessary filtration step to quantify the settled fraction. Thus, an increased w_{NaCl} does not

significantly ($p > 0.05$) influence settling, even at very high concentrations. This is in accordance with the results of Rommel and Helmreich [9] and Ying and Sansalone [29]. However, these experiments were not able to study the potential stratification present in SQIDs. In the experiments conducted at 10 °C, a significantly ($p < 0.05$) lower settled mass fraction was observed in contrast to the experiments at 21 °C, except for GBS. The settled mass fraction was 3% to 7% smaller at 10 °C in comparison to the experiments conducted at 21 °C.

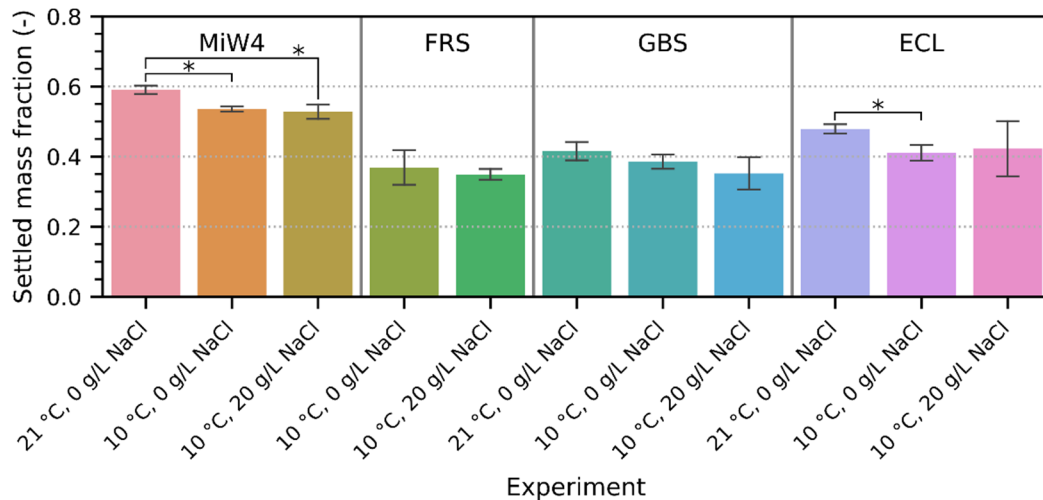


Figure 3. Settled mass fraction in the settling experiments with varying temperatures (21 and 10 °C) and NaCl concentrations (0 and 20 g/L); $n = 3$ for each experiment. The error bars indicate the standard deviation; the asterisks (*) indicate statistically significant differences between two experiments ($p < 0.05$). Experiment FRS 21 °C 0 g/L NaCl was not conducted due to low sample quantity.

As shown in Figure 4, the settled mass fraction increased with ρ_s and t . With increasing LOI, the settled mass fraction decreased. Thus, ρ_s can be considered as a function of LOI. This is in accordance with previous studies [15,20]. The settled mass fraction with respect to w_{NaCl} was not shown in this figure because only 10 °C experiments with $w_{NaCl} > 0$ were conducted; thereby, this figure could be easily misinterpreted.

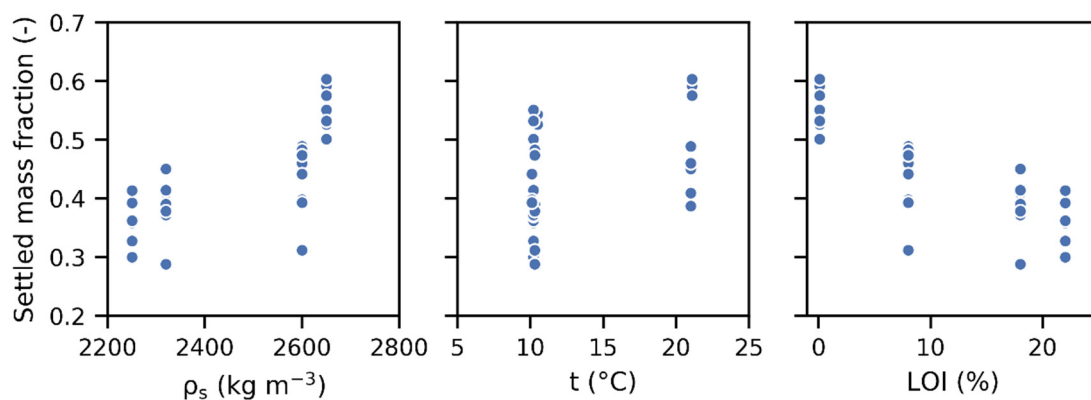


Figure 4. Settled mass fraction in the settling experiments with respect to ρ_s , t , and LOI; $n = 33$.

The utilized settling experiment method is simple to handle, but the results were very user-dependent (Figure S5); therefore, only the results of one executor should be compared. Nevertheless, the results of each setup and executor were consistent and able to show the effects of ρ_s , t , and w_{NaCl} . In addition, manual sampling can lead to a significant error. If the sampling were to be performed 30 s later, the settled mass fraction would increase by 0.03.

The VICAS protocol can be used to determine the settling velocity distributions of PM [12,55]; it has been comprehensively studied and increases the comparability of settling velocity distributions. However, the determination of the settling velocity was not the focus of this study. Furthermore, the UFT columns enabled an analysis of particle properties, such as contaminant content, with respect to settling velocity. Another promising method for the determination of settling velocity distributions and fractionation of particles with respect to settling velocity is the elutriation device proposed by Hettler et al. [26].

3.4. Validation of Settling Model

By means of using the results of the settling experiments, it was possible to validate the settling model for RDS, which is based on the PSD and ρ_s of the RSD, as well as t and w_{NaCl} of the fluid.

All settling models predicted the settled mass fraction with respect to t and w_{NaCl} very well (Figure 5 and Figure S6). Model A was already able to predict the settled fraction, with a mean absolute error of 0.054 and a maximum residual error of 0.143. Thus, this simple model, with input variables PSD, ρ_s , t , and w_{NaCl} , was sufficient to predict the outcome of the settling experiments. Model B considered additionally the withdrawn sample volume, which can extract nonsettled particles. However, it was not able to improve the prediction quality (mean absolute error of 0.059 and a maximum residual error of 0.161). Thus, the withdrawn sample volume seemed to be negligible. However, to meet quality assurance principles, the sample volume should be recorded. With consideration of the average particle shape of each RDS, Model C achieved a slight reduction of the mean absolute error to 0.050. The maximum residual error was 0.123. According to these results, the consideration of the nonsphericity of the particles does not considerably improve the prediction of RDS settling. If MiW4 is not considered, the mean absolute error of Models A and C are reduced to 0.050 and 0.037, respectively. The mean absolute error of Model B is increased to 0.064. The order of the predicted settled mass fractions by the models is Model C < Model A < Model B.

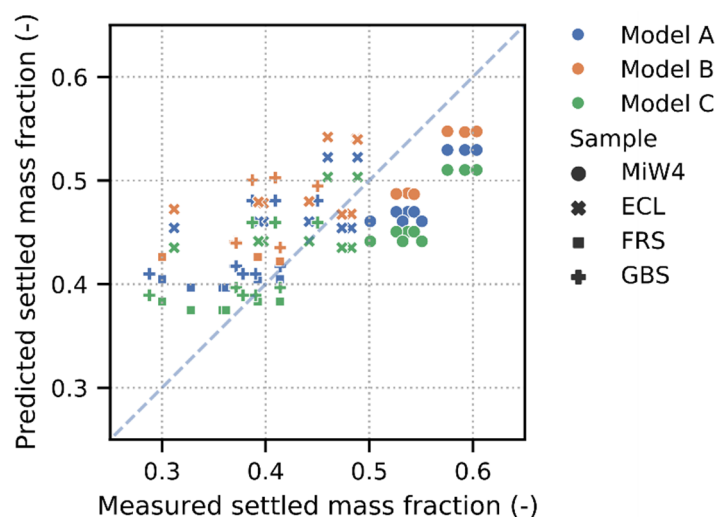


Figure 5. Comparison between measured and predicted settled mass fraction by Models A, B, and C of all samples (MiW4, ECL, FRS, and GBS); $n = 33$.

One unanticipated finding was that all models slightly underestimated the settled mass fraction of MiW4, while the settled mass of the nonartificial RDS was overestimated to a minor extent. As dynamic image analysis revealed that the PSDs of all samples, except for MiW4, differ from the Weibull PSD in the fine fraction, the deviation can be partly explained by the PSD. However, within the experiment duration of 4 min, it is mainly particles $d_{\text{eq}} > 60 \mu\text{m}$ that settle. Another possible explanation can be that even though all samples showed comparable mass fraction weighted median φ_{Riley} , MiW4 showed a narrower φ_{Riley} distribution with respect to d_{eq} (Figure 1b and Figure S3). Consequently, MiW4 settles

faster due to the smaller fraction of irregular-shaped particles, which exhibit lower settling velocities (Figure S7). Another source of bias was that the loss of particulate mass was considerably lower in the MiW4 experiments (1.8%) in contrast to the experiments with the real RDSs (3.6%). Thus, the overestimation of the settled fraction of the real RDSs can be partly explained by a mass loss during the experiments. Furthermore, the results are biased by the assumption of constant density with respect to particle size. The settled fractions of samples ECL and FRS, which mainly consisted of particles with $d_{eq} > 60 \mu\text{m}$, showed lower ρ_s than the average ρ_s of the whole sample. Hence, the mass of the settled fraction was overestimated, although this is not valid for GBS. With respect to these uncertainties in the experiments and modeling, the used models showed an acceptable error. Nevertheless, it must be emphasized that the proposed models are designed to evaluate influencing factors in settling column experiments under varying boundary conditions (PSD, ρ_s , t , w_{NaCl} , ϕ). Other approaches to model settling in full-scale SQIDs under dynamic conditions exist [21,22,56].

4. Conclusions

This study used preprocessed RDSs to reduce the effect of varying PSDs in order to assess effects caused by particle density, particle shape, temperature, and deicing salt concentration of the fluid.

Based on the experimental results, it was possible to validate and further develop the proposed method of Rommel and Helmreich [9], which is capable of modeling settling experiments with varying boundary conditions (PSD, ρ_s , t , w_{NaCl} , ϕ). All analyzed RDSs featured comparable particle shapes, independent from their origin. Consideration of the particle shape did not significantly improve the modeling results. Based on these findings, particle shape was negligible to describe the settling of RDS. Future studies are needed to verify this based on more samples of various sites. Furthermore, very fine particles, significantly smaller than $60 \mu\text{m}$, need to be studied as they potentially stay in suspensions for a long time and can be elutriated from SQIDs. This is of special importance due to the well-described high contaminant load in the fine particulate fraction.

The main limitation of the utilized settling experiments is that potentially occurring stratification in SQIDs cannot be reproduced. Thus, direct conclusions for SQIDs cannot be drawn. Future studies should assess the effect of stratification caused by temperature and salinity deviations using pilot or full-scale SQIDs and CFD modeling. Furthermore, road runoff underlies varying PM and hydraulic properties of intra- and inter-rain events. As RDS properties are site-specific, further investigations are necessary to predict site-specific PM properties.

Nevertheless, the gained knowledge on RDS properties can be used to evaluate future artificial RDSs for the assessment of SQIDs. In addition, the proposed model was able to deliver further insights into the relative contribution of the fluid and particle properties on the settling of RDS.

Supplementary Materials: The following are available online at <http://www.mdpi.com/2073-4441/12/11/3126/s1>. Figure S1: Bland–Altman plot for comparison of the two methods for the determination of the settled fraction (evaporation and filtration); the area between the dashed lines indicates the 95% confidence interval, $n = 9$; one outlier was removed. Figure S2: Particle size distribution of the preprocessed road-deposited sediments; fitted Weibull distribution for subsequent modeling of the sedimentation processes. Figure S3: 2D histogram of ϕ_{Riley} with respect to d_{eq} of all analyzed samples; color opacity indicates the density of counts; ECL $n = 130,986$, FRS $n = 211,209$, GBS $n = 134,392$, MiW4 $n = 57,973$. Figure S4: Mass fraction weighted histogram of the aspect ratios of the analyzed samples; ECL $n = 130,986$, FRS $n = 211,209$, GBS $n = 134,392$, MiW4 $n = 57,973$. Figure S5: Comparison of the experimental results of the settling experiments conducted by two different executers using the method described in this paper; $n = 27$. Figure S6: Settled mass fraction in the settling experiments; $n = 3$ for each experiment; the error bars indicate the standard deviation; experiment FRS, 21°C , 0g/L was not conducted due to low sample quantity; marker shows the predicted settled mass fraction determined by Models A and C. Figure S7: Settling velocity determined with the equations proposed by Haider and Levenspiel (Model C) with respect to particle diameter and sphericity at 20°C , ρ_s of MiW4, and $w_{\text{NaCl}} = 0$. Supplementary Material A: model code. Supplementary Material B: modeling input data.

Author Contributions: Conceptualization, S.H.R., L.G., and A.W.; methodology, S.H.R. and L.G.; software, S.H.R.; validation, S.H.R.; investigation, S.H.R. and L.G.; resources, A.W. and B.H.; data curation, S.H.R. and L.G.; writing—original draft preparation, S.H.R.; writing—review and editing, S.H.R., L.G., A.W., and B.H.; visualization, S.H.R.; supervision, A.W. and B.H.; project administration, A.W. and B.H.; funding acquisition, A.W. and B.H. All authors have read and agreed to the published version of the manuscript.

Funding: This research received no external funding.

Acknowledgments: We thank Matthias Schwibinger of the Institute of Urban Water Management and Hydromechanics, Frankfurt University of Applied Science, and Sebastian Schott of the Chair of Urban Water Systems Engineering, Technical University of Munich, for their assistance in the experiments.

Conflicts of Interest: The authors declare no conflict of interest.

Nomenclature

Symbol	Description
AR	Aspect ratio
C_D	Drag coefficient
CFD	Computational fluid dynamics
d	Particle diameter
d^*	Dimensionless particle diameter
D_c	Diameter of the smallest circumscribed circle
d_{eq}	Area equivalent circle diameter
D_i	Diameter of the largest inscribed circle
g	Acceleration due to gravity
LOI	Loss on ignition
PM	Particulate matter
PSD	Particle size distribution
RDS	Road deposited sediment
SCM	Stormwater control measure
SQID	Stormwater quality improvement device
t	Temperature of the fluid
w	Terminal settling velocity
w^*	Dimensionless settling velocity
w_{NaCl}	Mass fraction of the NaCl in the fluid
η_f	Dynamic viscosity of fluid
ν_f	Kinematic viscosity of fluid
ρ_f	Fluid density
ρ_s	Particle density
ϕ	Particle sphericity
φ_{Riley}	Riley circularity

References

1. Stone, M.; Marsalek, J. Trace metal composition and speciation in street sediment: Sault Ste. Marie, Canada. *Water Air Soil Pollut.* **1996**, *87*, 149–169. [[CrossRef](#)]
2. Sutherland, R.A.; Tolosa, C.A. Multi-element analysis of road-deposited sediment in an urban drainage basin, Honolulu, Hawaii. *Environ. Pollut.* **2000**, *110*, 483–495. [[CrossRef](#)]
3. Sutherland, R.A.; Tack, F.M.G.; Ziegler, A.D. Road-deposited sediments in an urban environment: A first look at sequentially extracted element loads in grain size fractions. *J. Hazard. Mater.* **2012**, *225–226*, 54–62. [[CrossRef](#)] [[PubMed](#)]
4. Loganathan, P.; Vigneswaran, S.; Kandasamy, J. Road-Deposited Sediment Pollutants: A Critical Review of their Characteristics, Source Apportionment, and Management. *Crit. Rev. Environ. Sci. Technol.* **2013**, *43*, 1315–1348. [[CrossRef](#)]
5. Murakami, M.; Nakajima, F.; Furumai, H. Size- and density-distributions and sources of polycyclic aromatic hydrocarbons in urban road dust. *Chemosphere* **2005**, *61*, 783–791. [[CrossRef](#)] [[PubMed](#)]
6. Zgheib, S.; Moillon, R.; Saad, M.; Chebbo, G. Partition of pollution between dissolved and particulate phases: What about emerging substances in urban stormwater catchments? *Water Res.* **2011**, *45*, 913–925. [[CrossRef](#)] [[PubMed](#)]
7. Dierkes, C.; Lucke, T.; Helmreich, B. General Technical Approvals for Decentralised Sustainable Urban Drainage Systems (SUDS)—The Current Situation in Germany. *Sustainability* **2015**, *7*, 3031–3051. [[CrossRef](#)]

8. Goonetilleke, A.; Lampard, J.-L. Chapter 3—Stormwater Quality, Pollutant Sources, Processes, and Treatment Options. In *Approaches to Water Sensitive Urban Design*; Sharma, A.K., Gardner, T., Begbie, D., Eds.; Woodhead Publishing: Cambridge, UK, 2019; pp. 49–74. ISBN 978-0-12-812843-5.
9. Rommel, S.H.; Helmreich, B. Influence of Temperature and De-Icing Salt on the Sedimentation of Particulate Matter in Traffic Area Runoff. *Water* **2018**, *10*, 1738. [[CrossRef](#)]
10. Roseen, R.M.; Ballesterio, T.P.; Houle, J.J.; Avellaneda, P.; Briggs, J.; Fowler, G.; Wildey, R. Seasonal Performance Variations for Storm-Water Management Systems in Cold Climate Conditions. *J. Environ. Eng.* **2009**, *135*, 128–137. [[CrossRef](#)]
11. Semadeni-Davies, A. Winter performance of an urban stormwater pond in southern Sweden. *Hydrol. Process.* **2006**, *20*, 165–182. [[CrossRef](#)]
12. Torres, A.; Bertrand-Krajewski, J.-L. Evaluation of uncertainties in settling velocities of particles in urban stormwater runoff. *Water Sci. Technol.* **2008**, *57*, 1389–1396. [[CrossRef](#)]
13. Kang, J.; Li, Y.; Lau, S.; Kayhanian, M.; Stenstrom, M. Particle Destabilization in Highway Runoff to Optimize Pollutant Removal. *J. Environ. Eng.* **2007**, *133*, 426–434. [[CrossRef](#)]
14. Gunawardana, C.; Egodawatta, P.; Goonetilleke, A. Role of particle size and composition in metal adsorption by solids deposited on urban road surfaces. *Environ. Pollut.* **2014**, *184*, 44–53. [[CrossRef](#)] [[PubMed](#)]
15. Kayhanian, M.; McKenzie, E.R.; Leatherbarrow, J.E.; Young, T.M. Characteristics of road sediment fractionated particles captured from paved surfaces, surface run-off and detention basins. *Sci. Total Environ.* **2012**, *439*, 172–186. [[CrossRef](#)]
16. McKenzie, E.; Wong, C.; Green, P.; Kayhanian, M.; Young, T. Size dependent elemental composition of road-associated particles. *Sci. Total Environ.* **2008**, *398*, 145–153. [[CrossRef](#)]
17. Gelhardt, L.; Huber, M.; Welker, A. Development of a Laboratory Method for the Comparison of Settling Processes of Road-Deposited Sediments with Artificial Test Material. *WaterAir Soil Pollut.* **2017**, *228*, 467. [[CrossRef](#)]
18. Li, Y.; Lau, S.-L.; Kayhanian, M.; Stenstrom, M.K. Particle size distribution in highway runoff. *J. Environ. Eng.* **2005**, *131*, 1267–1276. [[CrossRef](#)]
19. Li, Y.; Lau, S.; Kayhanian, M.; Stenstrom, M. Dynamic Characteristics of Particle Size Distribution in Highway Runoff: Implications for Settling Tank Design. *J. Environ. Eng.* **2006**, *132*, 852–861. [[CrossRef](#)]
20. Kayhanian, M.; Rasa, E.; Vichare, A.; Leatherbarrow, J. Utility of Suspended Solid Measurements for Storm-Water Runoff Treatment. *J. Environ. Eng.* **2008**, *134*, 712–721. [[CrossRef](#)]
21. Li, Y.; Kang, J.-H.; Lau, S.-L.; Kayhanian, M.; Stenstrom, M.K. Optimization of settling tank design to remove particles and metals. *J. Environ. Eng.* **2008**, *134*, 885–894. [[CrossRef](#)]
22. Spelman, D.; Sansalone, J.J. Is the Treatment Response of Manufactured BMPs to Urban Drainage PM Loads Portable? *J. Environ. Eng.* **2018**, *144*, 04018013. [[CrossRef](#)]
23. Lin, H.; Ying, G.; Sansalone, J. Granulometry of Non-colloidal Particulate Matter Transported by Urban Runoff. *Water Air Soil Pollut.* **2009**, *198*, 269–284. [[CrossRef](#)]
24. Laliberté, M.; Cooper, W.E. Model for calculating the density of aqueous electrolyte solutions. *J. Chem. Eng. Data* **2004**, *49*, 1141–1151. [[CrossRef](#)]
25. Laliberté, M. Model for Calculating the Viscosity of Aqueous Solutions. *J. Chem. Eng. Data* **2007**, *52*, 321–335. [[CrossRef](#)]
26. Hettler, E.N.; Gulliver, J.S.; Kayhanian, M. An elutriation device to measure particle settling velocity in urban runoff. *Sci. Total Environ.* **2011**, *409*, 5444–5453. [[CrossRef](#)] [[PubMed](#)]
27. Aiguier, E.; Chebbo, G.; Bertrand-Krajewski, J.-L.; Hedgest, P.; Tyack, N. Methods for determining the settling velocity profiles of solids in storm sewage. *Water Sci. Technol.* **1996**, *33*, 117–125. [[CrossRef](#)]
28. Michelbach, S.; Wöhrle, C. Settleable solids in a combined sewer system, settling characteristics, heavy metals, efficiency of storm water tanks. *Water Sci. Technol.* **1993**, *27*, 153–164. [[CrossRef](#)]
29. Ying, G.; Sansalone, J. Gravitational Settling Velocity Regimes for Heterodisperse Urban Drainage Particulate Matter. *J. Environ. Eng.* **2011**, *137*, 15–27. [[CrossRef](#)]
30. Blott, S.J.; Pye, K. Particle shape: A review and new methods of characterization and classification. *Sedimentology* **2008**, *55*, 31–63. [[CrossRef](#)]
31. Breakey, D.E.S.; Vaezi, G.F.; Masliyah, J.H.; Sanders, R.S. Side-view-only determination of drag coefficient and settling velocity for non-spherical particles. *Powder Technol.* **2018**, *339*, 182–191. [[CrossRef](#)]

32. Connolly, B.J.; Loth, E.; Smith, C.F. Shape and drag of irregular angular particles and test dust. *Powder Technol.* **2020**, *363*, 275–285. [[CrossRef](#)]
33. Wang, Y.; Zhou, L.; Wu, Y.; Yang, Q. New simple correlation formula for the drag coefficient of calcareous sand particles of highly irregular shape. *Powder Technol.* **2018**, *326*, 379–392. [[CrossRef](#)]
34. Bagheri, G.; Bonadonna, C. On the drag of freely falling non-spherical particles. *Powder Technol.* **2016**, *301*, 526–544. [[CrossRef](#)]
35. DIBt. *Teil 1: Anlagen zur dezentralen Behandlung des Abwassers von Kfz-Verkehrsflächen zur anschließenden Versickerung in Boden und Grundwasser; Zulassungsgrundsätze Niederschlagswasserbehandlungsanlagen*; Deutsches Institut für Bautechnik: Berlin, Germany, 2017.
36. Dierkes, C.; Welker, A.; Dierschke, M. Development of testing procedures for the certification of decentralized stormwater treatment facilities—Results of laboratory tests. *NOVATECH* **2013**, *2013*, 1–10.
37. Riley, N.A. Projection sphericity. *J. Sediment. Res.* **1941**, *11*, 94–95.
38. Bagheri, G.H.; Bonadonna, C.; Manzella, I.; Vonlanthen, P. On the characterization of size and shape of irregular particles. *Powder Technol.* **2015**, *270*, 141–153. [[CrossRef](#)]
39. Huber, M.; Welker, A.; Drewes, J.E.; Helmreich, B. Auftausalze im Straßenwinterdienst-Aufkommen und Bedeutung für dezentrale Behandlungsanlagen von Verkehrsflächenabflüssen zur Versickerung. *Abwasser* **2015**, *156*, 1138–1152.
40. Hilliges, R.; Endres, M.; Tiffert, A.; Brenner, E.; Marks, T. Characterization of road runoff with regard to seasonal variations, particle size distribution and the correlation of fine particles and pollutants. *Water Sci. Technol.* **2017**, *75*, 1169–1176. [[CrossRef](#)]
41. American Public Health Association; American Water Works Association; Water Environment Federation (Eds.) *Standard Methods for the Examination of Water and Wastewater*; American Public Health Association: Washington, DC, USA, 2017; ISBN 978-0-87553-287-5.
42. Virtanen, P.; Gommers, R.; Oliphant, T.E.; Haberland, M.; Reddy, T.; Cournapeau, D.; Burovski, E.; Peterson, P.; Weckesser, W.; Bright, J.; et al. SciPy 1.0: Fundamental algorithms for scientific computing in python. *Nat. Methods* **2020**, *17*, 261–272. [[CrossRef](#)]
43. The Pandas Development Team. *Pandas-Dev/Pandas: Pandas*; Zenodo: Geneva, Switzerland, 2020.
44. Hunter, J.D. Matplotlib: A 2D graphics environment. *Comput. Sci. Eng.* **2007**, *9*, 90–95. [[CrossRef](#)]
45. Waskom, M.; Botvinnik, O.; Ostblom, J.; Gelbart, M.; Lukauskas, S.; Hobson, P.; Gemperline, D.C.; Augspurger, T.; Halchenko, Y.; Cole, J.B.; et al. *Mwaskom/Seaborn: v0.10.1 (April 2020)*; Zenodo: Geneva, Switzerland, 2020.
46. Lee, D.H.; Min, K.S.; Kang, J.-H. Performance evaluation and a sizing method for hydrodynamic separators treating urban stormwater runoff. *Water Sci. Technol.* **2014**, *69*, 2122–2131. [[CrossRef](#)]
47. Selbig, W.R.; Fienen, M.N. Regression Modeling of Particle Size Distributions in Urban Storm Water: Advancements through Improved Sample Collection Methods. *J. Environ. Eng.* **2012**, *138*, 1186–1193. [[CrossRef](#)]
48. Haider, A.; Levenspiel, O. Drag coefficient and terminal velocity of spherical and nonspherical particles. *Powder Technol.* **1989**, *58*, 63–70. [[CrossRef](#)]
49. Cheng, N.-S. Comparison of formulas for drag coefficient and settling velocity of spherical particles. *Powder Technol.* **2009**, *189*, 395–398. [[CrossRef](#)]
50. Chhabra, R.P.; Agarwal, L.; Sinha, N.K. Drag on non-spherical particles: An evaluation of available methods. *Powder Technol.* **1999**, *101*, 288–295. [[CrossRef](#)]
51. Pedregosa, F.; Varoquaux, G.; Gramfort, A.; Michel, V.; Thirion, B.; Grisel, O.; Blondel, M.; Prettenhofer, P.; Weiss, R.; Dubourg, V.; et al. Scikit-learn: Machine learning in Python. *J. Mach. Learn. Res.* **2011**, *12*, 2825–2830.
52. Seabold, S.; Perktold, J. statsmodels: Econometric and statistical modeling with python. In Proceedings of the 9th python in science conference, Austin, TX, USA, 28 June–3 July 2010.
53. Kayhanian, M.; Givens, B. Processing and analysis of roadway runoff micro (<20 μm) particles. *J. Environ. Monit.* **2011**, *13*, 2720–2727.
54. Kreider, M.L.; Panko, J.M.; McAtee, B.L.; Sweet, L.I.; Finley, B.L. Physical and chemical characterization of tire-related particles: Comparison of particles generated using different methodologies. *Sci. Total Environ.* **2010**, *408*, 652–659. [[CrossRef](#)]

55. Chebbo, G.; Gromaire, M.-C. VICAS—An Operating Protocol to Measure the Distributions of Suspended Solid Settling Velocities within Urban Drainage Samples. *J. Environ. Eng.* **2009**, *135*, 768–775. [[CrossRef](#)]
56. Abrishamchi, A.; Massoudieh, A.M. Kayhanian Probabilistic modeling of detention basins for highway stormwater runoff pollutant removal efficiency. *Urban Water J.* **2010**, *7*, 357–366. [[CrossRef](#)]

Publisher’s Note: MDPI stays neutral with regard to jurisdictional claims in published maps and institutional affiliations.



© 2020 by the authors. Licensee MDPI, Basel, Switzerland. This article is an open access article distributed under the terms and conditions of the Creative Commons Attribution (CC BY) license (<http://creativecommons.org/licenses/by/4.0/>).